Document Version
Final published version

Citation (APA)
Fotouhi, S., Farrokhabadi, A., & Fotouhi, M. (2026). Simulation of Damage Sensing in Smart Self-Sensing Composites for Digital Design Integration. *Procedia Structural Integrity*, *80*, 310-320. https://doi.org/10.1016/j.prostr.2026.02.030

Available online at www.sciencedirect.com

ScienceDirect

Procedia Structural Integrity 80 (2026) 310–320

Structural Integrity
Procedia

www.elsevier.com/locate/procedia

Fracture, Damage and Structural Health Monitoring

Simulation of Damage Sensing in Smart Self-Sensing Composites for Digital Design Integration

Sakineh Fotouhi[a]*, Amin Farrokhabadi[b], Mohammad Fotouhi[c]

[a]University of the west of England, Bristol, BS16 1QY, UK
[b]The University of Nottingham Ningbo, Ningbo, 315100, China
[c]Delft University of Technology, Delft, 2628 CD, Netherlands

Abstract

Smart composite materials with integrated sensing layers are gaining attention for their potential to improve structural health monitoring and damage detection in high-performance applications. This study experimentally evaluates validated advanced simulation techniques to investigate impact-induced damage in such composites, with a particular focus on barely visible impact damage (BVID).

A refined finite element model is developed using user-defined cohesive materials to capture both matrix cracking and delamination, which are critical to understanding damage mechanisms associated with BVID. The model is applied to hybrid laminates incorporating surface-integrated sensing layers composed of ultra-high modulus carbon and S-glass fibres. These layers are designed to show visible signs of damage that can be correlated with internal failure mechanisms.

The simulation results are compared against experimental data, including C-scan imaging and surface inspections, to assess accuracy in predicting damage initiation, growth, and patterns. Particular attention is given to the effects of through-thickness compression and the interaction between different failure modes.

This work offers practical insights for reducing reliance on costly testing during the early stages of material and structural design for smart composites.

Keywords: Hybrid laminated composites; Barely visible impact damage; Low velocity impact; Self sensing, Finite element modelling

1. Introduction

Despite the advantages, such as lightweight and high strength-to-weight ratio (Sun and Hallett, 2018), composite materials have an important and yet unsolved limitation, i.e. susceptibility to impact damage (Siow and Shim, 1998). This can cause barely visible impact damage (BVID), which has a significant effect on the mechanical performance of laminates, especially the compressive strength, which may decrease by up to 60% compared with an undamaged laminate (Adsit and Waszczak, 1979; Lopes et al., 2009). BVID is induced by low-velocity impact (LVI) and is a critical design limiter for composite structures (Sun and Hallett, 2018). BVID can result in substantial internal damage without leaving a clear visible trace on the composite surface; therefore, it requires expensive and complex structural heath monitoring (SHM) systems, such as guided wave or vibration-based techniques to ensure operational safety.
Emerging self-sensing composites are being developing to show their own physical conditions, to avoid complex and extensive SHM. A recent study (Rev et al., 2019) presented a novel, purpose-designed thin interlayer glass/carbon-

---

* Corresponding author. *E-mail address: Sakineh.Fotouhi@uwe.ac.uk*

10.1016/j.prostr.2026.02.030

epoxy hybrid composite sensor concept that indicates structural overload by exhibiting a change in appearance when tensioned beyond a predefined strain value. A similar concept was successfully demonstrated to enhance the detection of BVID in composite structures (Fotouhi et al., 2023). However, this study is a feasibility study and offers only qualitative BVID detection. This highlights the need for new design solutions to develop quantitative, reliable, and integrated self-sensing capabilities for composite materials that can accurately detect and assess BVID. This will provide precise diagnostic data without requiring extensive structural health monitoring infrastructure. However, the development of such systems requires a thorough understanding of sensor–structure interaction, optimal sensor placement, and structural integration strategies. This paper develops a finite element (FE) model for designing such hybrid composite sensors. The model aims to develop FE modelling of the mechanical and sensing behaviour of the composite structure under various impacts, enabling optimisation of sensor architecture, interlayer positioning, and material combinations. By accurately predicting the sensor's response to BVID and associated strain fields, the FE modelling serves as a design tool to guide the development of next-generation self-sensing composites with quantitative diagnostic capabilities.

2. Design principles and experimental procedures

In this study, sensors are embedded on both sides of a conventional composite laminate (referred to as the reference (REF)) during the manufacturing process, as illustrated in Fig 1. The surface of the REF and sensor-embedded laminates appears uniformly black after fabrication, as light is fully absorbed by the opaque carbon beneath. Upon impact of the sensor-integrated laminate, structural damage occurs in a two-step process: first, cracks gradually develop at the carbon–glass interface; second, the glass layer undergoes splitting along the direction of the fibres. These changes disrupt the light path, causing it to scatter or reflect and thereby produce visible bright marks at the damaged locations. Notably, the area of visible reflection on the impacted face increases with higher levels of impact energy, enabling a qualitative visual assessment of damage severity.

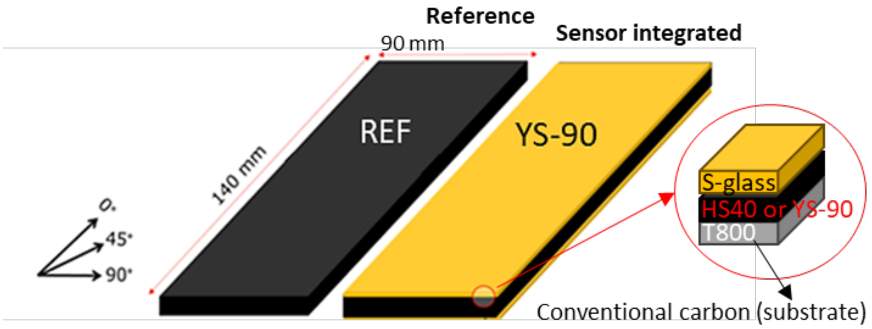

Fig 1. A carbon/epoxy composite (core laminate) with integrated impact detector sensors.

As listed in Table 1 and shown in Fig 1, the REF laminate was laid up in a quasi-isotropic (QI) stacking sequence, $[45_2/0_2/90_2/-45_2]_{4s}$, where 0° is the direction of unidirectional fibre orientation parallel to the long side of the plate. Unidirectional T800 carbon/MTM49-3 epoxy prepreg was used to fabricate the REF laminate as a rectangular plate with nominal in-plane dimensions of 140 × 90 mm and 4.64 mm thickness.

Table 1. Configuration of the specimens.

Specimen's name	Layup	Materials
REF	[45/0/90/-45]4S	QI T800
YS-90	[45/0/90/-45]4S with 90C/90G laminates	QI T800/YS-90A/S-glass

To estimate the impact energy required for delamination initiation, a Quasi-Static Indentation (QSI) test was conducted to determine suitable energy levels for subsequent LVI tests, considering that the critical energy in LVI is typically about 40% higher than that obtained from QSI (Sun and Hallett, 2017). The QSI and LVI tests also exhibit similar dent depths, back-surface crack patterns, and load-displacement responses (Fotouhi et al., 2021). The experimental setup for the QSI test is shown in Fig 2a. A 16 mm diameter steel hemispherical indenter was mounted on an Instron 8872 servo-hydraulic testing machine. The test followed ASTM D7136 (ASTM D7136 / D7136M and D7136/D7136M, 2012), where the specimen was clamped over a 125 × 75 mm window using four clamps. The QSI test was performed under displacement control at a constant rate of 2 mm/min. The critical energy level for delamination initiation was calculated from the area under the load–displacement curve up to the point of critical load. The values obtained from these tests are summarised in Table 2.

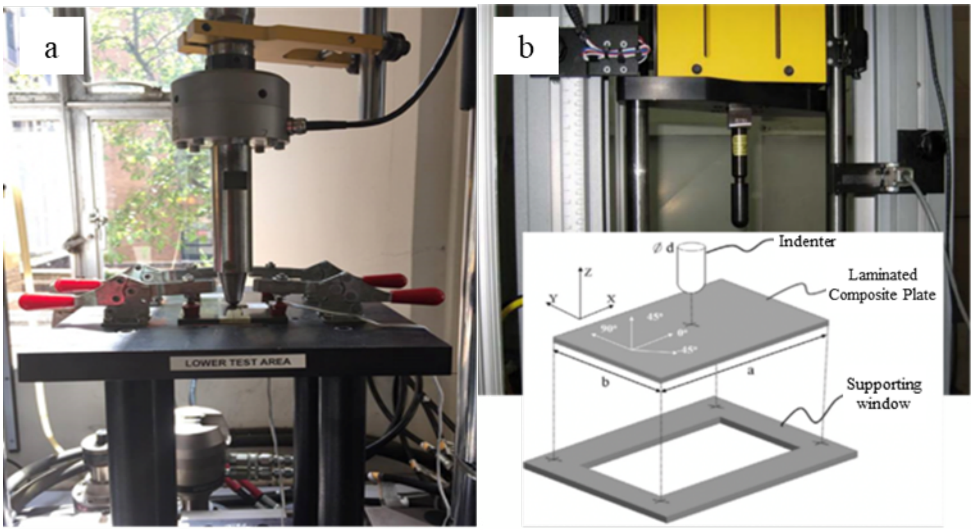

Fig 2. a) Test set-up for the QSI test; b) experimental configuration for the drop tower tests.

Table 2. Energy and stiffness values calculated from the load-displacement graphs

Sample name	Dimensions (mm)	Initial stiffness (kN/mm)	Absorbed elastic energy before initial delamination (J)	Estimated energy level for delamination initiation at impact tests (J)
REF	140 x 90 x 4.64	3.291	3.41	4.77

Once the critical energy level is estimated for the visual signal from the sensing layer, the LVI tests were carried out in a range near the critical energy level from Table 2. LVI tests were performed using Instron Dynatup 9250 HV drop-weight impact tower, and according to the ASTM D7136 standard (ASTM D7136 / D7136M, 2012). The samples were simply supported on a 125 x 75 window, with four rubber-tipped clamps, as illustrated schematically in Fig 2b. The impact load and displacement were measured by a single accelerometer inside the tup, and the measured data were processed by a 4 kHz filter of the console software to reduce the noise and oscillations.

The selection of the thickness, materials, and layup of the sensor is done by calculating the critical load levels for mid-plane delamination, because delamination initiates at above and below adjacent interfaces of the symmetry plane (Sun et al., 2016). If the critical strain level in the critical load for delamination initiation of the REF laminate is calculated, then the innermost carbon layer of the sensor can be chosen to match the critical strain. The critical load level occurs well before the maximum load and it is usually indicated with a load drop in the load-displacement curves from experimental results (see Fig 3).

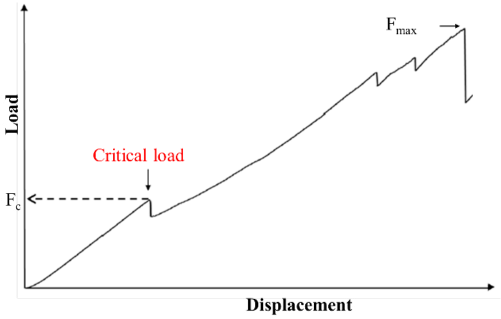

Fig 3. A typical overall graph for a QI laminated composite under LVI and QSI (Fotouhi et al., 2021).

To investigate the strain levels experienced by the samples, strain gauges are used to measure the strain level of the REF sample in the centre on the back face, and on the front face and in a 10 mm distance from the centre of the sample, allowing enough space for the indenter while preventing it from damaging the strain gauge. It is worth noting that the strain distribution under the indenter (front face) is higher than that measured experimentally because of the distance between the strain gauge and the centre of the sample. The results of the load versus time and strain versus time are illustrated in Fig 4. The figure shows that the strain level for delamination initiation on the back face of the samples is 0.8%. This strain level can be used to choose appropriate grades of the carbon and glass layers for the hybrid sensor to get activated at a desired strain level. Hence, YS-90 thin ply, with a strain to failure of 0.5% is chosen to reveal BVID, as it is lower than the REF laminate's critical strain for internal delamination initiation.

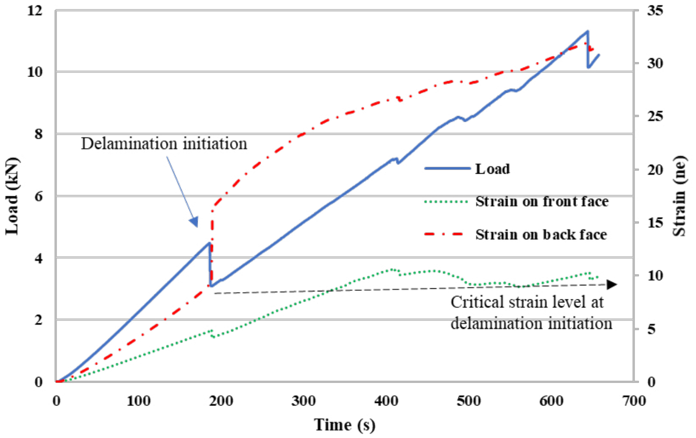

Fig 4. Back face strain and front face strain of the REF laminate under QSI

The hybrid sensor, made from S-glass/YS-90A-Carbon (YS-90), was integrated into the REF sample, and cured at the same time as the REF laminate. The sensors were integrated into the front and back faces of the REF laminate, and each was composed of a single layer of the YS-90 carbon prepreg with 90˚ orientation, that was sandwiched between the REF laminate and a single layer of an S-glass prepreg with 90˚ orientation. Characteristics of the utilised prepregs are summarised in Table 3.

Table 3. Characteristics of the utilised pre-pregs

Pre-preg type	Cured nominal thickness (mm)	E11 ply (GPA)	Tensile failure strain (%)
T800/MTM49-3 epoxy	0.145	163	1.70
S-glass/913 epoxy	0.155	45.7	5.50

YS-90A/epoxy (E9026A)	0.07	520	0.50

Three series of drop tower tests with different energy levels, starting from levels associated with no visible damage and increasing to higher energy levels, were performed on the investigated samples. Using the estimated critical elastic energy level from in Table 2, the minimum energy level was set to 3 J. Load-displacement graphs for REF samples impacted at different energy levels, from 3 J to 8 J, are presented in Fig 5. Similar to the indentation results, the impacted samples show a load-drop associated with the initiation of delamination. As can be seen from Fig 5, there is no load-drop associated with the 3 J and 6 J impacts. This means that these energy levels do not cause any damage to the samples, whereas 8 J causes a load drop that is related to the initiation of delamination. For surface-visible damage analysis, an EPSON scanner was used to take clear images of both the front face (impacted face) and the back face of the investigated samples. Fig 6 shows the EPSON scans and C-scans for samples subjected to energy levels of 3, 6, and 8 J. The C-scan reveals significant delamination damage for the 8 J energy level, where the delamination size is slightly higher in the REF sample compared to the sensor-integrated samples. However, there is no change in the appearance of the REF sample in the front and back faces. It is shown that the sensors work satisfactorily and visually indicate the BVID location, and that there are direct relationships between visible damage and internal hidden damage initiation observed by C-scan.

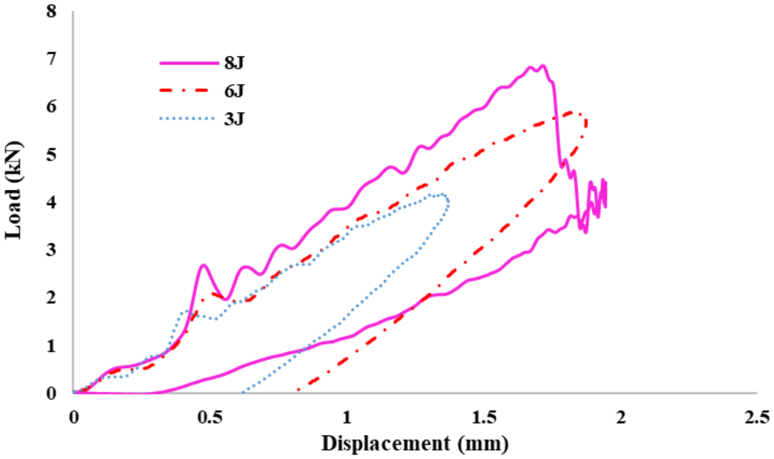

Fig 5. Load-displacement plots under drop-weight impact for the REF sample at 3 different energy levels.

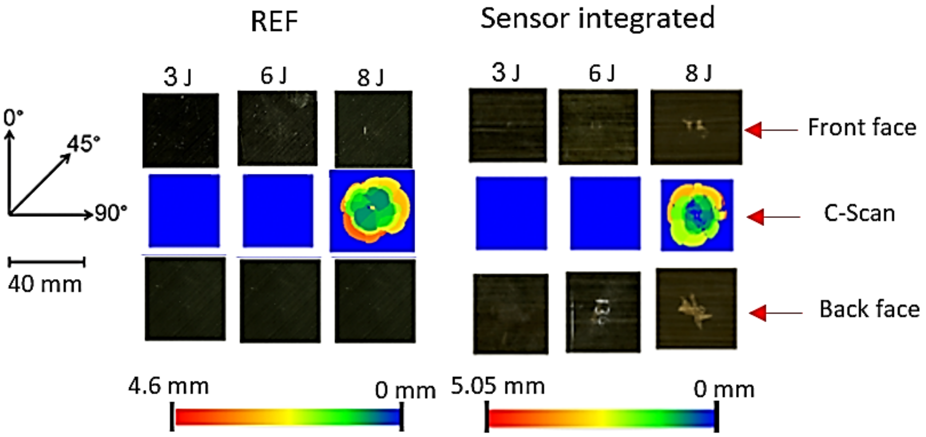

Fig 6. Images of the impacted samples using EPSON scanner and C-scan, taken from the front face and back.

3. FE modelling

The developed FE model aims to find the stress and strain distribution on the back face and front face of the samples where the sensing layers are located. In addition, the maximum shear stress distribution and its location are evaluated to identify when BVID occurs. This will help to understand the interaction between damage mechanisms in the sensing layers and BVID. First, the FE model is validated against a previous study by Sun et al. (Sun and Hallett, 2017) on IM7 carbon/epoxy QI laminates with the stacking sequence of $[45_2/0_2/90_2/\text{-}45_2]_{2S}$ under low LVI. Validation is done in terms of damage initiation, damage pattern and mechanical response. After the REF sample's model is validated with experimental results, the final model integrated with sensing layers, comprising a single layer of unidirectional ultra-high modulus (UHM) carbon/epoxy and S-glass/epoxy materials, is developed.

The FE method is developed using the commercial software of LS-Dyn. The modelling strategy is presented, followed by model validation against experimental results of the REF sample at two different impact energy levels. The damage area, damage pattern, and strain distribution along the surface are also investigated. A schematic of the impactor, support window, and composite plate assembly is illustrated in Fig 7. The support window and the impactor were represented as 3D solid rigid bodies, with constrained displacements and rotations except for the z (thickness) direction of the impactor. The interaction between the composite plate and the impactor is defined using automatic contact, while a tied contact is used for the support window. A friction coefficient of 0.3 is applied to the relevant interfaces. The initial velocity and impactor's mass are defined as the loading inputs.

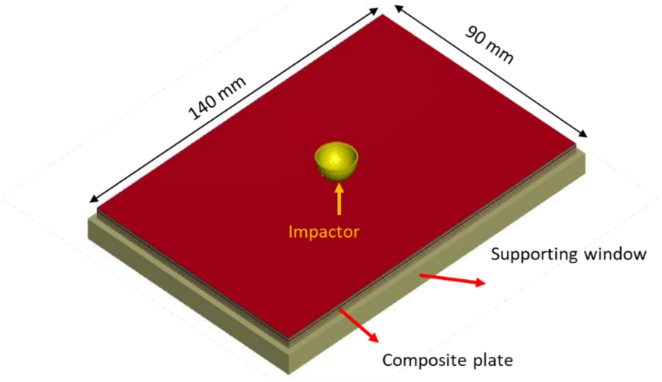

Fig 7. Schematic of the assembly for the FE simulation.

Each of the plies is modelled with orthotropic elastic materials with constant stress solid elements. To consider delamination between the plies, thin cohesive interfaces with 0.005 mm thickness are modelled. Delamination initiation and propagation patterns are not predicted well using the ultimate failure criteria of the existing materials in LS-DYNA library, such as Mat 45/55 (Jackson et al., 2011). Hence, the plies are defined by elastic orthotropic properties with no in-plane or interlaminar damage initiation criteria. Because delamination is controlled by the direction of transverse matrix cracks (Fotouhi et al., 2020a), six splits in the fibre direction were embedded into each ply to track the matrix crack initiation and its progress. A quadratic stress-based failure criterion dictates the damage onset in mixed-mode loading and damage progression is controlled by two damage evolution laws including power and Benzeggagh-Kenane laws. Although the formulation of the cohesive elements is modified to consider the enhancement effect of through-thickness compression on shear behaviour. The shear strength and Mode II critical energy release rate are assumed to increase linearly by a material-dependent enhancement factor, in the presence of through-thickness compressive stress (Sun et al., 2016). Through-thickness compression effects are implemented into the LS-DYNA solver via a user material subroutine. For the subroutine, Mode II critical fracture energy and shear behaviour are increased by the enhancement factor $of\,\phi$=0.74, as shown in Equation 1, where G_{IIC} is the critical energy release rate for mode II loading. $\sigma^*_{IIn} and\ G_{IIC_n}$ are the enhanced Mode II strength and critical energy release rate (Sun et al., 2016).

$$\begin{aligned} \sigma_{IIn}{}^{*} &= \sigma_{II}{}^{*} - \varphi\sigma_{I} \qquad When \quad \sigma_I < 0 \\ G_{IICn} &= G_{IIC}\left(\frac{\sigma_{IIn}{}^{*}}{\sigma_{II}{}^{*}}\right) \end{aligned} \tag{1}$$

Table 4 shows the material types and assigned element formulation options. Table 5 shows the material properties used for the model. The material properties for T800/MTM49-3 are chosen/calculated from (Stodieck et al., 2017). The material properties for cohesive elements are mainly chosen from (Sun et al., 2016). To verify the results with the experiments, the shear strength (σ_{II}) used in (Sun et al., 2016) is arbitrarily changed from 90 MPa to 70 MPa to improve correlation. This change is considered to be reasonable, as there are also much smaller values (up to 7 MPa) reported for the shear strength to model epoxy matrix using cohesive elements (Moheimani et al., 2020). A wide range of empirical elastic moduli is also reported for FE simulation of epoxy matrix, from 0.8 GPa (Moheimani et al., 2020) to 10^5 GPa (Jalalvand et al., 2014). In this study, 30 MPa is used as it provides the best fit with the experiment.

Table 4. Material definition and formulation in LS-DYNA.

	Material	**Element formulation options (section)**
Plies	Mat_Orthotropic_Elastic (MAT_02)	Reduced integration 8-noded brick elements (Type-1)
Interface	Mat_Cohesive_Mixed_Mode (MAT_138)	8-noded, 4-point cohesive element (Type-19)
Support window	Mat-Rigid, Constrained x, y & z+ Constrained x, y & z rotation	Reduced integration 8-noded brick elements (Type-1)
Impactor	Mat-Rigid, Constrained x & y+ Constrained x, y & z rotation	Reduced integration 8-noded brick elements (Type-1)

Table 5. Material properties used for the FE simulation.

Ply property (T800/MTM49-3) (Stodieck et al., 2017)									
Density (g/cm^3)	E_{11} (GPa)	E_{22} (GPa)	E_{33} (GPa)	v_{12}	v_{13}	V_{23}	G_{12} (GPa)	G_{13} (GPa)	G_{23} (GPa)
1.60	163	6.8	6.8	0.28	0.28	0.4	3.4	3.4	2.5
Split and interface cohesive properties (Sun et al., 2016)									
$E_I{}^* = E_{II}{}^* = 30\,GPa \quad G_{IC} = 0.2N/mm \quad G_{IIC} = 0.8N/mm$									
$\sigma_I = 60\,MPa\ \sigma_{II}{}^{(1)} = 70MPa \quad \rho = 1g/cm^3$									
*The values are chosen to fit the experiments within the range that is used in the literature reviews									
Impactor and support window made from steel									
Density (g/cm3) = 7.8 Young's modulus (GPa) = 210 Poisson's ratio=0.3									

A very small mesh size underneath the impactor is used to precisely model the progressive damage inside composites. This will help to achieve a reasonable stress and strain distribution in the back face and front face of the samples where the sensing layers are located. The FE model took an average of 4 days for each of the runs using high-performance computers with 16 SMP (multi-processing) and 16 G memory tokens.

Experimental results showed no damage under 6J energy level in the REF and sensor integrated samples. Hence, the FE modelling is done for 8J and 12J to see the capacity of the FE model in evaluating the induced damage mechanisms. The load-displacement behavior of the developed FE model and experimental results are compared in Fig 8, where the simulation results are multiplied by the scaling factor of 0.99 ($(4.77/4.795)^{1.5}$) (Fotouhi et al., 2020a) to account for increased thickness of the simulated model caused by the 31 cohesive interfaces. A Reasonable agreement for the elastic stiffness, maximum load, and their respective displacements is observed between the experimental and simulated results as summarized in Table 6.

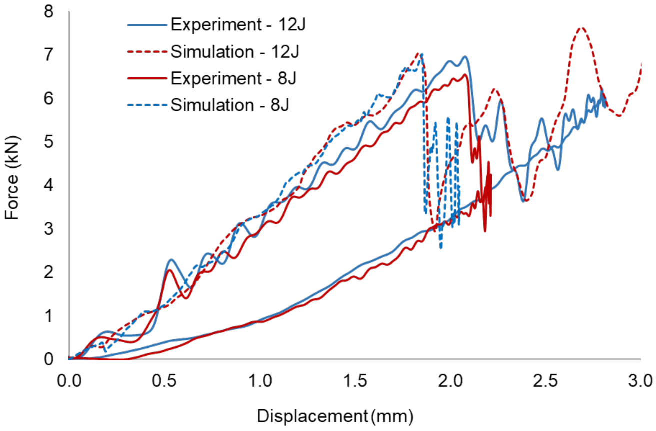

Fig 8. Load displacement response for the REF sample under 8 J and 12 J energy levels

Table 6. Comparing simulated and experimental results for different energy levels.

Energy level		Maximum load (kN)	Error (%)	Displacement at maximum load (mm)	Error (%)	Elastic stiffness (GPa)	Error (%)
12 J	Experiment	6.96	0.71	2.08	11.05	3.83	12.53
	Simulation	7.01		1.85		3.35	
8 J	Experiment	6.55	6.82	2.08	11.54	3.14	17.80
	Simulation	7.03		1.84		3.82	

The damage area and damage patterns for each of the interfaces are also studied using the FE model. Fig 9 shows the induced damage for both the experiment and simulations. The simulated damaged area for both energy levels is slightly larger than the experimental areas. Delamination is often controlled by the direction of transverse matrix cracks (Fotouhi et al., 2020b). In this study, the elastic modulus defined for embedded cohesive splits is relatively small (30 GPa), which might explain the larger delamination area in the simulations. The difference between the simulations and experiments for the 8J and 12J cases might also be due to rate-dependent effects in the simulation (Huang et al., 2022) results, which is not investigated here.

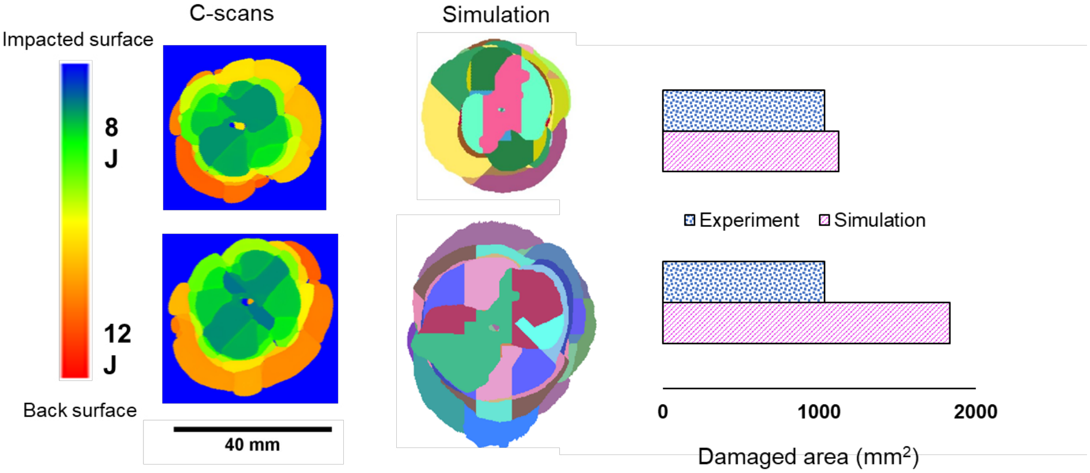

Fig 9. Comparing the induced damage area in FE model and experiments for two energy levels in the REF samples.

The FE model captures the pattern and direction of delamination determined by the fibre directions in the adjacent plies. It should be noted that due to the high compression effect underneath the impactor, the first interface usually does not delaminate (Fotouhi et al., 2020a). Hence, a simple elastic cohesive material (with no damage initiation) is allocated to the first interface (i.e., the interface between the first 45° and 0° plies).

Fig 10 and Fig 11 illustrate the strain distribution over the impacted (front) and non-impacted (back) surfaces of the simulated REF sample alongside the experimental visual images of the sensor-integrated samples. The simulated strain distribution results on the back face are in good agreement with the experimental results reported in Fig 4. Fig 10 and Fig 11 show that the sensing layers experienced damage and revealed a visual sign, i.e. bright areas, where strain distribution exceeds the compression or tension strain to failure of the sensing HS40 and YS-90A layers. For the back face, the visual damage pattern is only because of the damage induced by the tensile strain. However, for the front face, the visual damage pattern is mainly due to compressive strain with some minor contribution from the tensile strain in areas near the impactor. Due to the lower strain to failure of the YS-90A, its visual damage pattern is more obvious compared to HS40 sample. For example, the applied strain did not exceed the critical strain on the front face of the HS40 sample, and therefore there is barely visible damage on the front face at 8 J as shown in Fig 11.

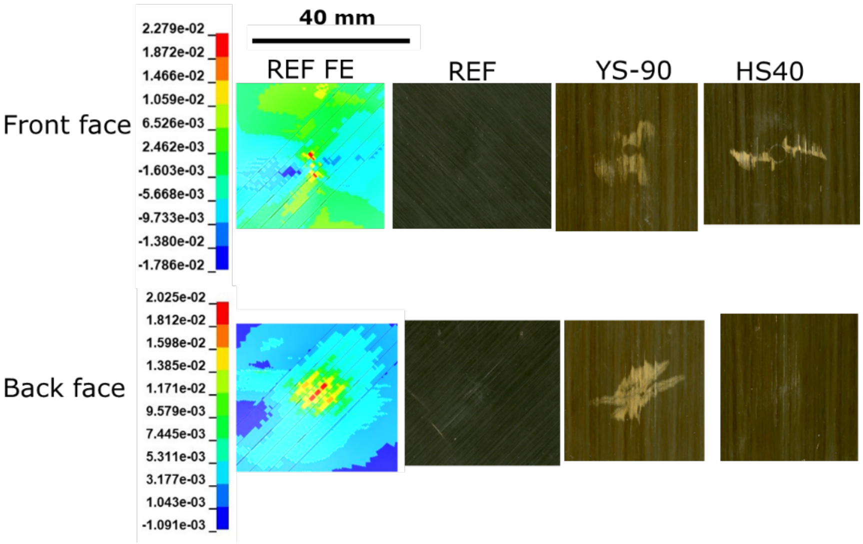

Fig 10. Strain distribution over the back and front face of the samples under 12 J energy level at damage initiation.

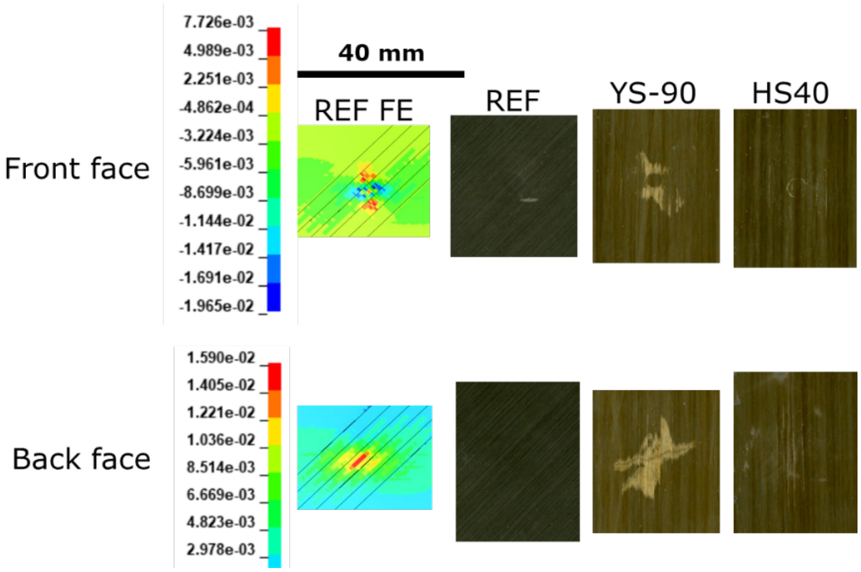

Fig 11. Strain distribution over the back and front face of the samples under 8 J energy level at damage initiation.

4. Conclusion

A developed finite element (FE) model successfully explained the visible damage observed in the hybrid composite sensors. This was achieved by comparing the strain-to-failure of the sensing material with the strain distribution results from the FE analysis. The model not only helped identify the cause of damage but also offers potential for designing hybrid composite sensors by analysing strain distributions along the sensing layer for different substrates and selecting materials with appropriately low strain-to-failure. By aligning damage initiation in the sensing layer with the displacement associated with BVID in the substrate, the failure can be effectively engineered. The FE simulation accurately replicated experimental observations, showing strong agreement in damage patterns and maximum load values, along with a reasonable match in elastic response. Moreover, it provided valuable insights into the damage area, delamination behaviour, and interfacial responses that are difficult and time-consuming to capture experimentally. However, refinements are needed in the user-defined material properties to better account for the enhancement of shear behaviour due to through-thickness compression. Further investigation is also required to assess how the enhancement factor depends on impact energy. A key challenge remains in accurately modelling the outermost layers beneath the impactor, where the simulation predicts premature damage initiation.

Acknowledgements

The authors are grateful to Professor Michael Wisnom from School of Civil, Aerospace and Design Engineering, University of Bristol, for his expert insights and thoughtful comments on this work and contributing to its development.

References

Adsit, N.R., Waszczak, J.P., 1979. Effect of Near-Visual Damage on the Properties of Graphite/Epoxy., in: ASTM Special Technical Publication. pp. 101–117. https://doi.org/10.1520/stp36905s

ASTM D7136 / D7136M, 2012. Standard Test Method for Measuring the Damage Resistance of a Fiber-Reinforced Polymer Matrix Composite to a Drop-Weight Impact Event. ASTM International United States.

ASTM D7136 / D7136M, D7136/D7136M, A., 2012. Standard test method for measuring the damage resistance of a fiber-reinforced polymer matrix composite to a drop-weight impact event, Annual

Book of ASTM Standards.

Fotouhi, M., Damghani, M., Leong, M.C.M.C., Fotouhi, S., Jalalvand, M., Wisnom, M.R.M.R., 2020a. A comparative study on glass and carbon fibre reinforced laminated composites in scaled quasi-static indentation tests. Compos Struct 245. https://doi.org/10.1016/j.compstruct.2020.112327

Fotouhi, M., Damghani, M., Leong, M.C.M.C., Fotouhi, S., Jalalvand, M., Wisnom, M.R.M.R., 2020b. A comparative study on glass and carbon fibre reinforced laminated composites in scaled quasi-static indentation tests. Compos Struct 245. https://doi.org/10.1016/j.compstruct.2020.112327

Fotouhi, S., Jalalvand, M., Wisnom, M.R., Fotouhi, M., 2023. Smart hybrid composite sensor technology to enhance the detection of low energy impact damage in composite structures. Compos Part A Appl Sci Manuf 172, 107595. https://doi.org/10.1016/j.compositesa.2023.107595

Fotouhi, S., Khoshravan Azar, M.R., Fotouhi, M., 2021. Achieving robust acoustic emission-based damage characterization of scaled laminated composites under indentation. Express Polym Lett 15, 839–852. https://doi.org/10.3144/expresspolymlett.2021.67

Huang, J., Zhang, Chenxu, Wang, J., Zhang, Chao, 2022. On the applicability of rate-dependent cohesive zone models in low-velocity impact simulation. Eng Fract Mech 271. https://doi.org/10.1016/j.engfracmech.2022.108659

Jackson, K.E., Littell, J.D., Fasanella, E.L., 2011. Simulating the Impact Response of Composite Airframe Components, in: 13th International LS-DYNA Users Conference. pp. 1–26.

Jalalvand, M., Czél, G., Wisnom, M.R., 2014. Numerical modelling of the damage modes in UD thin carbon/glass hybrid laminates. Compos Sci Technol 94, 39–47. https://doi.org/10.1016/j.compscitech.2014.01.013

Lopes, C.S.S., Camanho, P.P.P., Gürdal, Z., Maimí, P., González, E.V., Seresta, O., Coquet, Y., Guerdal, Z., Camanho, P.P.P., Thuis, B., 2009. Low-velocity impact damage on dispersed stacking sequence laminates. Part II: Numerical simulations. Compos Sci Technol 69, 926–936.

Moheimani, R., Sarayloo, R., Dalir, H., 2020. Failure study of fiber/epoxy composite laminate interface using cohesive multiscale model. Advanced Composites Letters 29. https://doi.org/10.1177/2633366X20910157

Rev, T., Jalalvand, M., Fuller, J., Wisnom, M.R., Czél, G., 2019. A simple and robust approach for visual overload indication - UD thin-ply hybrid composite sensors. Compos Part A Appl Sci Manuf 121, 376–385. https://doi.org/10.1016/j.compositesa.2019.03.005

Siow, Y.P., Shim, V.P.W., 1998. An experimental study of low velocity impact damage in woven fiber composites. J Compos Mater 32, 1178–1202. https://doi.org/10.1177/002199839803201203

Stodieck, O., Francois, G., Heathcote, D., Zympeloudis, E., Kim, B.C., Rhead, A.T., Cleaver, D., Cooper, J.E., 2017. Experimental validation of tow-steered composite wings for aeroelastic design. 17th International Forum on Aeroelasticity and Structural Dynamics, IFASD 2017 2017-June.

Sun, X.C., Hallett, S.R., 2018. Failure mechanisms and damage evolution of laminated composites under compression after impact (CAI): Experimental and numerical study. Compos Part A Appl Sci Manuf 104, 41–59. https://doi.org/10.1016/j.compositesa.2017.10.026

Sun, X.C., Hallett, S.R., 2017. Barely visible impact damage in scaled composite laminates: Experiments and numerical simulations. Int J Impact Eng 109, 178–195. https://doi.org/10.1016/j.ijimpeng.2017.06.008

Sun, X.C., Wisnom, M.R., Hallett, S.R., 2016. Interaction of inter- and intralaminar damage in scaled quasi-static indentation tests: Part 2 - Numerical simulation. Compos Struct 136, 727–742. https://doi.org/10.1016/j.compstruct.2015.09.062